Nano Energy 69 (2020) 104438

Contents lists available at ScienceDirect

Nano Energy

journal homepage: http://www.elsevier.com/locate/nanoen

Full paper

Highly efficient copper-rich chalcopyrite solar cells from DMF molecular solution

Jingjing Jiang [a], Rajiv Giridharagopal [b], Erin Jedlicka [b], Kaiwen Sun [c], Shaotang Yu [a], Sanping Wu [a], Yuancai Gong [a], Weibo Yan [a], David S. Ginger [b,**], Martin A. Green [c], Xiaojing Hao [c,***], Wei Huang [a], Hao Xin [a,*]

[a] Key Laboratory for Organic Electronics and Information Displays & Jiangsu Key Laboratory for Biosensors, Institute of Advanced Materials (IAM), Jiangsu National Synergetic Innovation Centre for Advanced Materials (SICAM), Nanjing University of Posts &Telecommunications, 9 Wenyuan Road, Nanjing, 210023, China
[b] Department of Chemistry, University of Washington, Seattle, WA, 98195, USA
[c] School of Photovoltaic and Renewable Energy Engineering, University of New South Wales (UNSW), Sydney, New South Wales, Australia

ARTICLE INFO

Keywords:
CIGS
Chalcopyrite
Cu-rich
High pressure
Selenization
DMF

ABSTRACT

Theoretical calculation suggests Cu-rich chalcopyrite absorbers contain less defects and have potential to achieve better performance than Cu-poor absorbers. However, this has not been demonstrated due to the detrimental $Cu_{2-x}Se$ impurity remaining in the absorber. Here, we report highly efficient Cu-rich chalcopyrite solar cells by selenizing dimethylformamide molecular precursor solution processed precursor films under high Ar pressure. Characterizations using XRD, Raman, SEM, TEM, c-AFM, PL, and glow discharge optical emission spectroscopy (GDOES) show high pressure selenization enables high quality Cu-rich chalcopyrite absorber materials with stoichiometric composition, smooth surface, high conductivity, and $Cu_{2-x}Se$ free grain boundaries, leading to efficient $CuIn(S,Se)_2$ and $Cu(In,Ga)(S,Se)_2$ devices with power conversion efficiency of 14.5% and 15.2%, both are the best performing chalcopyrite solar cells from non-hydrazine solutions. Our results demonstrate high Ar pressure selenization is a new strategy to fabricate high quality Cu-rich absorber which has great potential to further improve chalcopyrite solar cell efficiency.

1. Introduction

Copper indium gallium selenide ($Cu(In,Ga)Se_2$, CIGS) is one of the high performing thin film technology with efficiency close to single crystal silicon solar cell [1]. The absorbers of high performing CIGS solar cells can be fabricated by annealing the deposited precursor films with element Se or H_2Se atmosphere (so called selenization) [2,3]. It is generally agreed that the grain growth of CIGS as well as $CuInSe_2$ (CIS) during selenization follows a few steps [4–8]: (a) Se or H_2Se reacts with metal to form liquid phases such as $Cu_{2-x}Se$, In_4Se_3, or InSe; (b) Cu, In and Ga diffuse into the liquid media and form CIS/CIGS nuclei; (c) CIS/CIGS grains grow. A Cu-rich ([Cu]/[In] or [Cu]/([In]+[Ga])>1) precursor condition favours formation of $Cu_{2-x}Se$ and facilitates elements (In, Ga, Cu, S) diffusion and grain growth [4,5,9]. Both experimental and theoretical calculation results suggest that CIS/CIGS absorbers fabricated under Cu-rich conditions have higher carrier concentration and less defects or lower defect concentration than Cu-poor absorbers and thus have potential to achieve higher efficiency [10]. However, excess $Cu_{2-x}Se$ within the absorber can act as recombination centres or even cause shunt paths if it remains in the grain boundaries [11,12]. Therefore, all the absorbers of previously reported high efficiency CIS/CIGS solar cells are fabricated under Cu-poor conditions. Even with Cu-poor conditions, an etching procedure is generally required to eliminate residue $Cu_{2-x}Se$ as well as other impurities on the surface [12–14]. However, $Cu_{2-x}Se$ formed deep in the film cannot be etched out and thus Cu-rich absorbers have not demonstrated high performance yet.

We previously reported copper indium sulfoselenide (CISSe) solar cells with the absorber fabricated from Cu-poor ([Cu]/[In] = 0.85) dimethylformamide (DMF) molecular solution and found that

* Corresponding author.
** Corresponding author.
*** Corresponding author.
E-mail addresses: dginger@uw.edu (D.S. Ginger), xj.hao@unsw.edu.au (X. Hao), iamhxin@njupt.edu.cn (H. Xin).

https://doi.org/10.1016/j.nanoen.2019.104438
Received 2 November 2019; Received in revised form 25 December 2019; Accepted 25 December 2019
Available online 30 December 2019

selenization pressure greatly affects absorber property and device performance [15,16]. Performing selenization under 1 atm Ar pressure (0.10 MP) resulted in poor CISSe absorber with only 0.01% power conversion efficiency (*PCE*) whereas selenization under higher Ar pressure (0.16 MP) achieved $Cu_{2-x}Se$ free CISSe absorber with 10.3% *PCE* without any additional surface etching. The results indicate the great potential of high pressure selenization in achieving high quality chalcopyrite absorbers. In this work, we have investigated how selenization pressure affects the photovoltaic property of DMF solution based CISSe absorbers with the [Cu]/[In] ratios of 0.85, 0.95, 1.05, and 1.20. Our results show that under the two selenization pressures (0.10 and 0.16 MP) investigated, CISSe solar cell performance gradually increases from Cu-poor ([Cu]/[In] = 0.85) to slightly Cu-rich (1.05) whilst decreases with further increase of [Cu]/[In] to 1.20. More importantly, solar cells with the absorber selenized under 0.16 MP exhibits much higher efficiency than that under 0.10 MP at every single composition investigated. Characterization including XRD, Raman, SEM, TEM, conductive atomic force microscopy (c-AFM), glow discharge optical emission spectroscopy (GDOES) and low temperature PL spectra show that the combination of Cu-rich ([Cu]/[In] = 1.05) composition and high pressure selenization results in high quality absorber material with $Cu_{2-x}Se$ free grain boundaries. Using $(NH_4)_2S$ solution to etch out surface $Cu_{2-x}Se$, a dense defect-free surface is formed which facilitates epitaxial deposition of CdS. A champion solar cell with an efficiency of 14.5% has been achieved from CISSe absorber fabricated with Cu-rich ([Cu]/[In] = 1.05) absorber. By alloying the absorber with 25% Ga, Cu-rich CIGSSe solar cell with an efficiency of 15.2% has been obtained under the same device fabrication condition. To the best of our knowledge, this is the first time that highly efficient CIS/CIGS solar cells are fabricated from Cu-rich absorbers.

2. Results and discussion

2.1. Effect of [Cu]/[In] ratio and selenization pressure on absorber property and device performance

Fig. 1 shows the current density-voltage (*J-V*) and external quantum efficiency (*EQE*) curves of the best-performing CISSe solar cells fabricated from DMF solutions with [Cu]/[In] ratios of 0.85, 0.95, 1.05 and 1.20 and selenized under 0.10 MP (condition A) and 0.16 MP (condition B) Ar pressures, which are respectively named CIS-0.85A, CIS-0.95A, CIS-1.05A and CIS-1.20A for condition A and CIS-0.85B, CIS-0.95B, CIS-1.05B and CIS-1.20B for condition B. Due to the non-optimized mask and contact fabrication condition, the grid of our solar cell device covers 10.5% of the total device area (Supporting Information, Fig. S1), and the *J-V* curves and efficiency are based on active area rather than total area unless otherwise noticed. The average device parameters, including current density (J_{sc}), open circuit voltage (V_{oc}), fill factor (*FF*), *PCE*, series resistance (R_s), and shunt resistance (R_{sh}), with standard deviations based on 10 pixels of the best devices are summarized in Table 1. For both conditions, with the increase of [Cu]/[In] ratio from 0.85 to 1.05, *PCE* increases with the main enhancement gained from V_{oc} and *FF*, when the [Cu]/[In] ratio further increases to 1.20, all device parameters decrease with the V_{oc} drops the most. Devices under

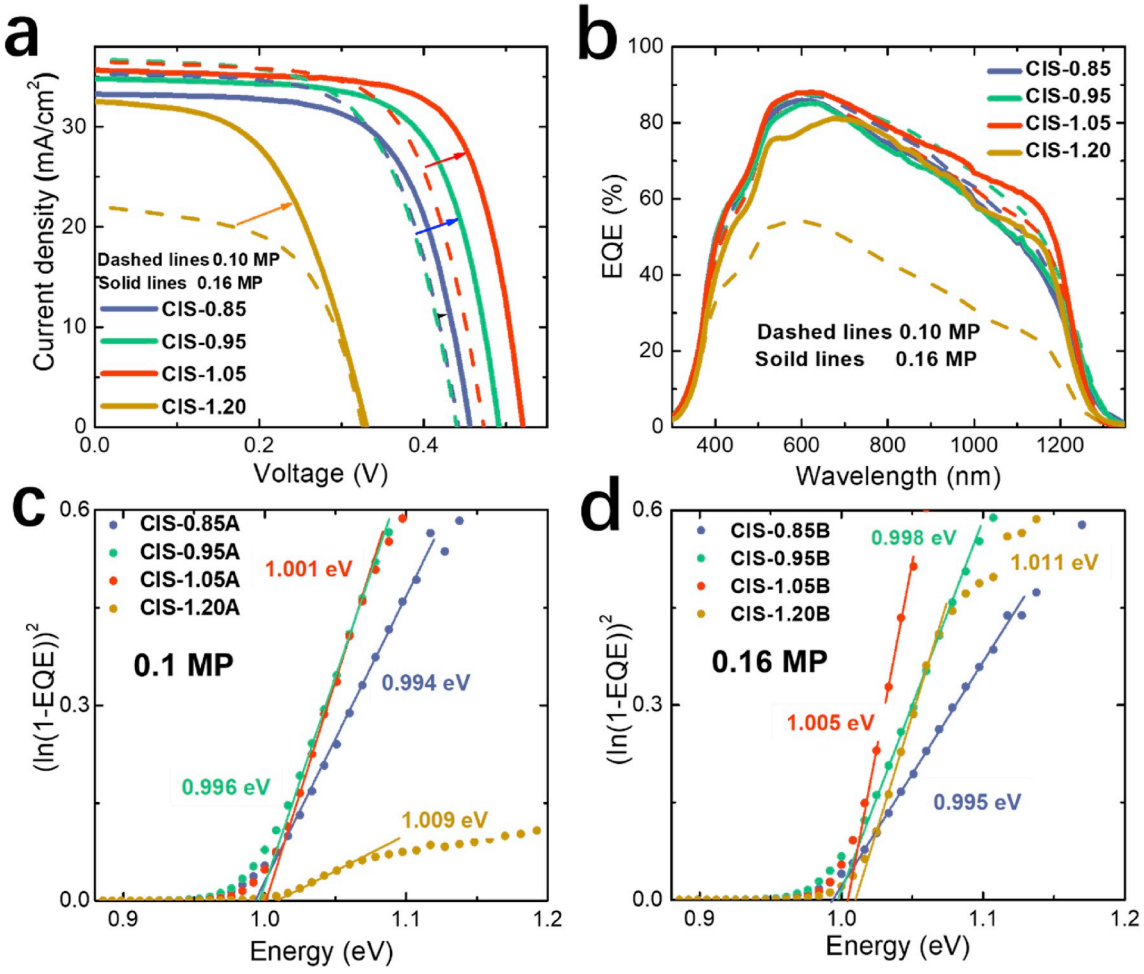

Fig. 1. (a) *J-V* curves, (b) *EQE*, and (c, d) bandgap estimation of the best performing CISSe solar cells with the absorber selenized under condition A (0.10 MP, dashed lines) and condition B (0.16 MP, solid lines) with the [Cu]/[In] ratios of 0.85, 0.95, 1.05 and 1.20.

Table 1
Summary of device parameters of the CISSe solar cells with the absorber fabricated under different conditions.

[a]Pressure (MP)	Device	[b][Cu]/[In]	E_g (eV)	J_{sc} (mA/cm^2)	V_{oc} (V)	*FF* (%)	[c]PCE_{ave} (%)	[d]PCE_{max} (%)	R_s (Ω cm^2)	R_{sh} (Ω cm^2)
0.10	CIS-0.85A	0.89	0.994	34.68 ± 1.14	0.433 ± 0.009	61.29 ± 1.65	9.21 ± 0.48	9.79	2.1 ± 0.3	421 ± 173
	CIS-0.95A	0.97	0.996	37.08 ± 1.74	0.437 ± 0.006	61.14 ± 0.75	9.86 ± 0.32	9.86	1.9 ± 0.1	351 ± 120
	CIS-1.05A	1.02	1.001	36.28 ± 2.57	0.470 ± 0.005	63.77 ± 1.45	10.83 ± 0.32	11.25	2.0 ± 0.1	564 ± 417
	CIS-1.20A	1.10	1.009	24.87 ± 2.11	0.345 ± 0.015	55.64 ± 1.48	4.16 ± 0.11	4.26	1.7 ± 0.1	97 ± 14
0.16	CIS-0.85B	0.85	0.995	33.46 ± 1.33	0.453 ± 0.002	65.27 ± 0.64	9.89 ± 0.34	9.96	1.7 ± 0.1	458 ± 274
	CIS-0.95B	0.95	0.998	34.07 ± 1.78	0.477 ± 0.013	65.56 ± 2.17	10.65 ± 0.60	11.66	1.7 ± 0.1	1357 ± 236
	CIS-1.05B	1.05	1.005	34.66 ± 1.46	0.516 ± 0.004	70.50 ± 0.60	12.61 ± 0.80	13.29	1.5 ± 0.1	869 ± 386
	CIS-1.20B	1.06	1.011	29.42 ± 2.33	0.324 ± 0.008	51.06 ± 1.98	4.87 ± 0.59	5.62	3.1 ± 0.6	663 ± 631

[a] 0.1 MP and 0.16 MP corresponds to condition A and condition B respectively.
[b] Measured by EDX.
[c] PCE_{ave}: average efficiency based on 10 pixels.
[d] PCE_{max}: maximum efficiency of each condition.

condition B show significantly improved V_{oc} and *FF* with slightly reduced J_{sc} than condition A at every composition, resulting in overall much higher efficiency. A *PCE* of 11.25% was obtained from CIS-1.05A with J_{sc}, V_{oc} and *FF* of 36.51 mA/cm^2, 0.470 V and 65.54%, whereas CIS-1.05B achieved 13.29% *PCE* with J_{sc}, V_{oc} and *FF* of 35.69 mA/cm^2, 0.520 V and 71.54%. The V_{oc}, *FF* and *PCE* of device CIS-1.05B are respectively enhanced by 11%, 9% and 18% compared to device CIS-1.05A. One CIS-1.05B device with 108 nm MgF_2 anti-flection coating (ARC) was certified by National Institute of Metro, China to have a total area efficiency of 12.2% (Supporting Information). The active area efficiency of the certified device was 13.5% measured in house, higher than 13.1% efficient CISSe solar cell fabricated from DMF solution with composition gradient in the literature [17].

All devices have similar *EQE* response within the depletion range at wavelength below 800 nm except for CIS-1.20A and CIS-1.20B. At longer wavelength from 800 nm to 1200 nm, which reflects the quality of the absorber bulk, the highest carrier collection efficiency was observed in CIS-1.05B among all the solar cells. For [Cu]/[In] = 1.20 composition, although both devices suffer from interface and bulk recombination, device CIS-1.20B (yellow solid line) exhibits much better *EQE* response in the whole wavelength range than CIS-1.20A (yellow dashed line) and close to other devices except for the depletion range, indicating device CIS-1.20A has higher fraction of interface recombination compared to device CIS-1.20B. The current density integrated from the *EQE* (Table S1) agrees well with the values measured by the *J-V* characterization. The *EQE* data further confirm high pressure (0.16 MP) selenization enables high quality absorber material especially for Cu-rich conditions. In addition, when [Cu]/[In] ratio increases from 0.85 to 1.20, we observe a better collection for the near-infrared region from the *EQE* measurement (Fig. 1b). The bandgap of the CISSe absorber, extracted from the *EQE* data (Fig. 1c and d and Table 1) also slightly increases from 0.994 to 1.009 eV for 0.10 MP films and 0.995–1.011 eV for 0.16 MP films, consistent with the compositional changes observed with GDOES and will be discussed later.

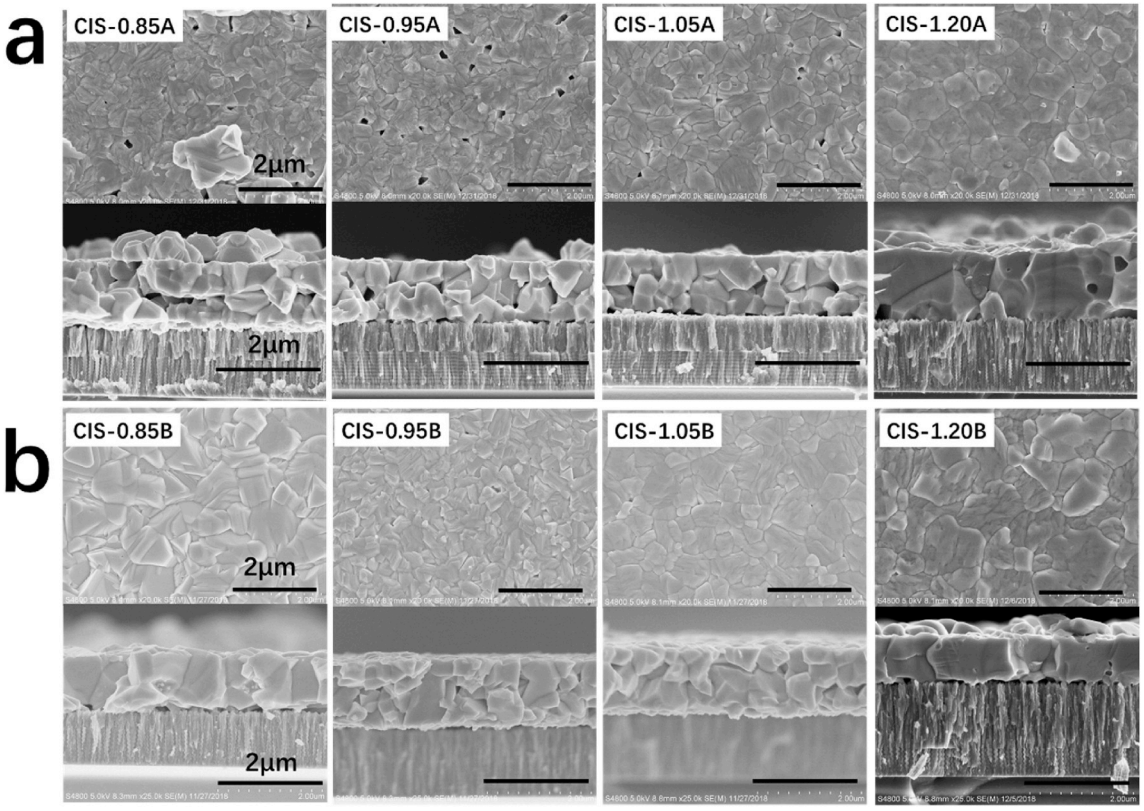

Fig. 2. (a) Surface and (b) cross-section SEM images of CISSe absorber films selenized under 0.10 MP (condition A) and (b) 0.16 MP (condition B) pressure. All films were etched in 20% $(NH_4)_2S$ solution for 15 min to get rid of surface impurities.

Top view and cross-section scanning electron microscopy (SEM) images of the CISSe absorber films are shown in Fig. 2. Under condition A (0.10 MP), with the increase of [Cu]/[In] ratio from 0.85 to 1.20, films become denser with less voids. Cross-section images show all films have comparable grain size except for CIS-1.20A which has much larger and more densely packed grains. In addition, micrometre size scattered grains are found on the surface of CIS-0.85A, making the cross-section appear as a tri-layer film. All films under condition B (0.16 MP) are denser than the ones of condition A without large voids within the absorber layers. Although there are still scattered grains on the surface of CIS-0.85B (Fig. 2a, first image), they are much less than CIS-0.85A. While we observe no obvious change in grain size for films prepared under condition A, the grains of films CIS-0.85B and CIS-1.20B are larger than films CIS-0.95B and CIS-1.05B. The densely packed larger grains lead to thinner film thickness due to less grain boundaries. Importantly, the surfaces of films from condition B are smoother than condition A films. The surface root-mean square roughness (RMS) measured by AFM (Supporting Information, Fig. S2) are 140 nm for CIS-0.85B and only 20 nm for CIS-1.05B, in consistent with the observation of smaller grains in CIS-1.05B.

The much better morphology of absorbers fabricated under condition B is obviously resulted from the high pressure selenization. According to our previous work [15] and another report [5], under condition A (0.10 MP), Se has high vapour pressure and a large amount of liquid Se penetrates from the film surface to the whole film where $Cu_{2-x}Se$ nuclei form and further grow to large grains. The diffusion of Cu and In around the nuclei leaves voids and results in loosely connected grains in low [Cu]/[In] ratio (e.g. 0.85) films. With the increase of the [Cu]/[In] ratio, more $Cu_{2-x}Se$ facilitates the growth of larger grains and denser films. Under condition B (0.16 MP), the evaporation of Se is suppressed and only limited Se is condensed into liquid where $Cu_{2-x}Se$ nuclei are formed. For CIS-0.85B, due to limited $Cu_{2-x}Se$ nuclei, the grain growth relies on up diffusion of Cu and In, which results in continuous films and leaves voids at the absorber/$MoSe_2$ interface. With [Cu]/[In] ratio increasing from 0.95 to 1.05, some $Cu_{2-x}Se$ can penetrate into the film and form more nuclei, resulting in smaller grains and denser films. When [Cu]/[In] further increases to 1.20, the extra $Cu_{2-x}Se$ enables growth of small grains to large ones.

The chemical composition of the absorber films measured by EDX (Table S2 and Table 1) shows that with the increase of [Cu]/[In] ratios from 0.85 to 1.05 in the precursor solution, the [Cu]/[In] ratios in the absorber films also consistently increase from 0.85 (CIS-0.85B absorber) to 1.05 (CIS-1.05B absorber) but only slightly increase from 1.05 (CIS-1.05B absorber) to 1.06 (CIS-1.20B absorber). Within the accuracy of EDX measurement, the [Cu]/[In] ratios in Cu-rich CIS-1.05B and CIS-1.20B films are very close to unit, confirming the stoichiometric composition is reached at the [Cu]/[In] ratio of 1.05 and the excess $Cu_{2-x}Se$ on the surface was etched away by $(NH_4)_2S$ solution. In addition, the (S + Se)/(Cu + In) ratio in Cu-poor films (CIS-0.85 and CIS-0.95) is slightly above unit due to the Cu deficiency. Furthermore, all films exhibit low S content with the S/(S + Se) ratios varying from 0.03 to 0.06, revealing sufficient selenization.

XRD patterns and Raman spectra of the two sets of absorber films are shown in Fig. 3. All films exhibit sharp diffractions that can be indexed to $CuInSe_2$ (JCPDS#40–1487). The crystalline grain sizes of the films are comparable in the range of 42–52 nm except for CIS-1.20A which has grain sizes of 107 nm (Supporting Information, Table S3). From the enlarged (112) diffractions shown in Fig. 3a, it can be clearly seen that with [Cu]/[In] ratio increasing from 0.85 to 1.05, the (112) peak shifts to smaller angle for both conditions, which indicates an increased size of the unit cell. The lattice constant *a*, *b* and *c* of the CISSe calculated based on (112) and (220) peaks together with that of $CuIn_3Se_5$ and $CuInSe_2$ are shown in Table S4. Both *a* and *c* values gradually increase with the increasing [Cu]/[In] ratio from 0.85 to 1.05 and stop further increasing at 1.20. The smaller unit cell in Cu-poor films can be explained by more Se–V_{Cu} bonds, which are about 10% shorter than Se–Cu bonds [18,19]. The XRD results are consistent with the EDX data and further confirm the stoichiometric composition of CIS-1.05 films.

Raman spectra (Fig. 3b) show that all absorber films exhibit characteristic A_1 (171 cm^{-1}) and B_2/E (209 cm^{-1}) Raman modes of CISe [20,21]. As expected, the vibrational mode from order defect compounds (such as $CuIn_3Se_5$, $Cu_3In_5Se_9$) [22,23] at 151 cm^{-1} is observed in both Cu-poor films of CIS-0.85A and CIS-0.85B. Raman shift at 260 cm^{-1}, arising from vibrational mode of $Cu_{2-x}Se$, is detected in 0.10 MP selenized CIS-1.05A and CIS-1.20A films but absent in 0.16 MP selenized CIS-1.05B and CIS-1.20B. Because all films were soaked in $(NH_4)_2S$ solution for 15 min before Raman measurements to remove $Cu_{2-x}Se$ defects from the surface, the absence of the Raman signal of $Cu_{2-x}Se$ reveals the extra $Cu_{2-x}Se$ in Cu-rich CIS-1.05B and CIS-1.20B mainly exists at film surface which was etched away during the etching process. On the

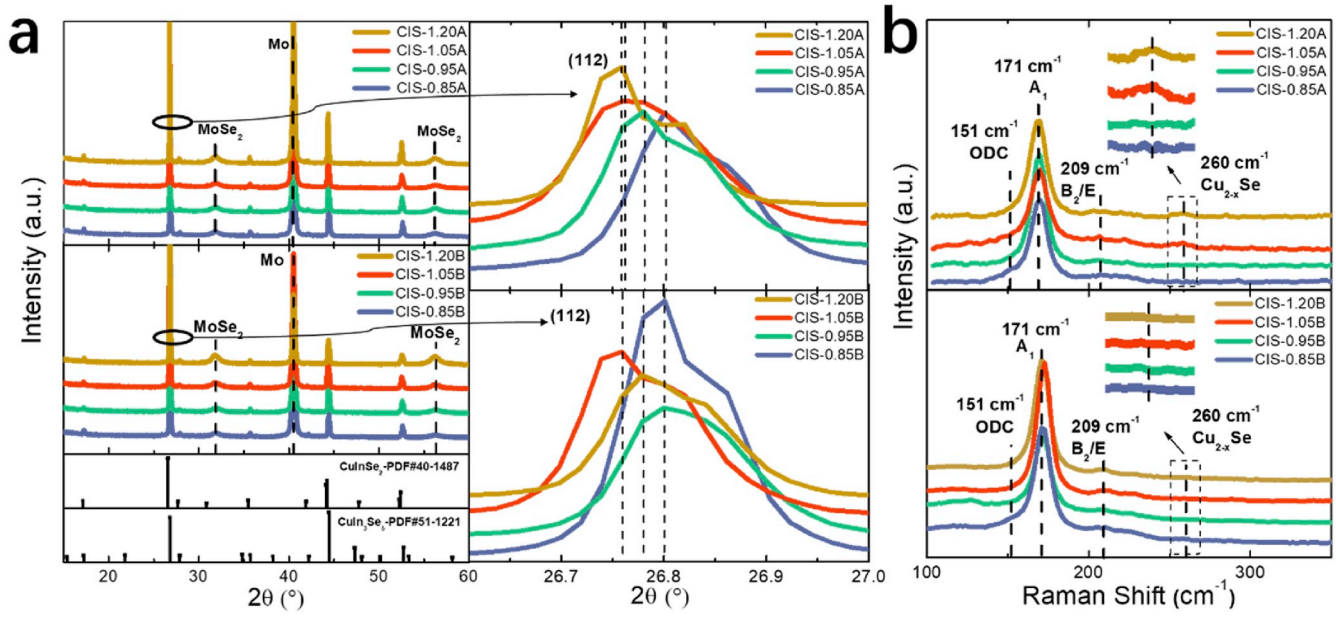

Fig. 3. XRD (a) and Raman (b) spectra of CISSe absorber films selenized under condition A and condition B. The (112) diffractions are enlarged to show peak shift. Inset of (b): the enlarged Raman signal of $Cu_{2-x}Se$ at 260 cm^{-1}. All the films were soaked in 20 wt% $(NH_4)_2S$ solution for 15min to etch surface impurities.

contrast, for CIS-1.05A and CIS-1.2A films, $Cu_{2-x}Se$ also exist in film bulk or grain boundaries which cannot be completely removed by etching, which is supported by the Raman data measured with different etching time (Supporting Information, Fig. S3). The remaining $Cu_{2-x}Se$ can act as recombination centre or even form shunting paths for solar cell, consistent with the lower device performance of CIS-1.05A (CIS-1.20A) than CIS-1.05B (CIS-1.20B).

2.2. Comparison of high pressure selenized Cu-rich and Cu-poor CISSe absorbers

To understand the mechanism of improved photovoltaic performance of Cu-rich CIS-1.05B than Cu-poor CIS-0.85B absorbers, here after, we will focus on investigating compositional and electrical property difference between CIS-0.85B and CIS-1.05B by employing glow discharge optical emission spectroscopy (GDOES), TEM, c-AFM, and temperature dependent photoluminescence.

Compositional depth profiles and Cu/In, Na/Se, (Cu + In)/(S + Se) and S/(S + Se) ratios of CIS-0.85B and CIS-1.05B absorber films measured via GDOES are shown in Fig. 4. Secondary Ion Mass Spectrometry (SIMS) shows similar trends as GDOES (Supporting Information, Fig. S4). As expected, CIS-1.05B film has higher [Cu]/[In] (Fig. 4b) and (Cu + In)/(S + Se) (Fig. 4e) ratios than CIS-0.85B due to higher Cu content. Both films show quite uniform Cu, In and Se composition distribution in the bulk with slightly higher S concentration towards film back for CIS-0.85B (Fig. 4f) which we attribute to different film growth as discussed above. The early formed dense top layer in the top-down grain growth Cu-poor (CIS-0.85) film prevents S release whereas a uniform grain growth in Cu-rich CIS-1.05B has a relatively less dense morphology for S to escape. The significant compositional difference between the two films is near the film surface. The surface of the CIS-0.85B absorber shows a stronger Cu-depletion at the very surface compared to the CIS-1.05B absorber as indicated by the fact that the [Cu]/[In] ratio in the bulk of the former absorber is about twice as high as that at the very surface (Fig. 4b). Na exhibits a reverse trend to [Cu]/[In] in the surface of CIS-0.85B absorber (Fig. 4c). On the contrast, the surface of CIS-1.05B absorber has a consistent (even slightly higher) [Cu]/[In] ratio to the bulk (Fig. 4b) and a decrease of Na content (Fig. 4c) towards the surface. In addition, CIS-1.05B absorber contains more Na than CIS-0.85B in the film bulk. It is known that Na can stay at the grain boundary and grain interior [24]. We proposed that Na mainly occupies Cu vacancies near the surface of Cu-poor CIS-0.85B and very likely stays at grain boundaries in CIS-0.85B bulk and stoichiometric CIS-1.05B absorber. We attribute the higher Na in CIS-1.05B than CIS-0.85B to its much smaller grains and thus more grain boundaries (Fig. 2b). It was proposed that Na can passivate donor-like defects at grain boundaries, such as In_{Cu} or Se vacancies, increasing net hole concentration and improving device performance [25–27], which agrees with the measured *PCEs* for the two devices.

The dark field TEM images of CIS-0.85 and CIS-1.05B lamellae and the EDX line scans at CdS/CISSe interfaces and interior grain boundaries are shown in Fig. 5. A few features can be seen from the TEM images: (1) the average grain size in CIS-0.85 film is larger than CIS-1.05B, agreeing with the observed grain sizes in SEM (Fig. 2b). However, the top layer of CIS-1.05B film is only formed by densely packed large grains whereas the top layer of CIS-0.85 contains small and loosely packed grains with rough surface. (2) The rough surface of CIS-0.85B causes non-uniform deposition of CdS (Fig. 5a, solid circle) and a defective buffer/absorber interface, whereas CIS-1.05B has a uniform, sharp and epitaxial-like interface. (3) CIS-0.85B has impurities (Fig. S5) and voids within the absorber (dotted circle in Fig. 5a) whereas CIS-1.05B is almost impurity-free (note: the voids in films are due to dropped small grains during lamellar thinning). (4) Large voids exist between the absorber and Mo in both films. The higher quality buffer/absorber interface and absorber of CIS-1.05B might reduce recombination and thus improve device performance.

The line scans cross the ZnO/CdS/CISSe interfaces (Fig. 5b) clearly show Cd diffusion into the absorber for both films. However, the diffusion depth is 23 nm for CIS-0.85B but only 12 nm for CIS-1.05B. The much longer diffusion depth in CIS-0.85B is obviously due to the very Cu-poor surface (Fig. 4b) where the Cu vacancies may not only assist Cd diffuse [28] but also provide space for Cd to occupy. For Cu rich

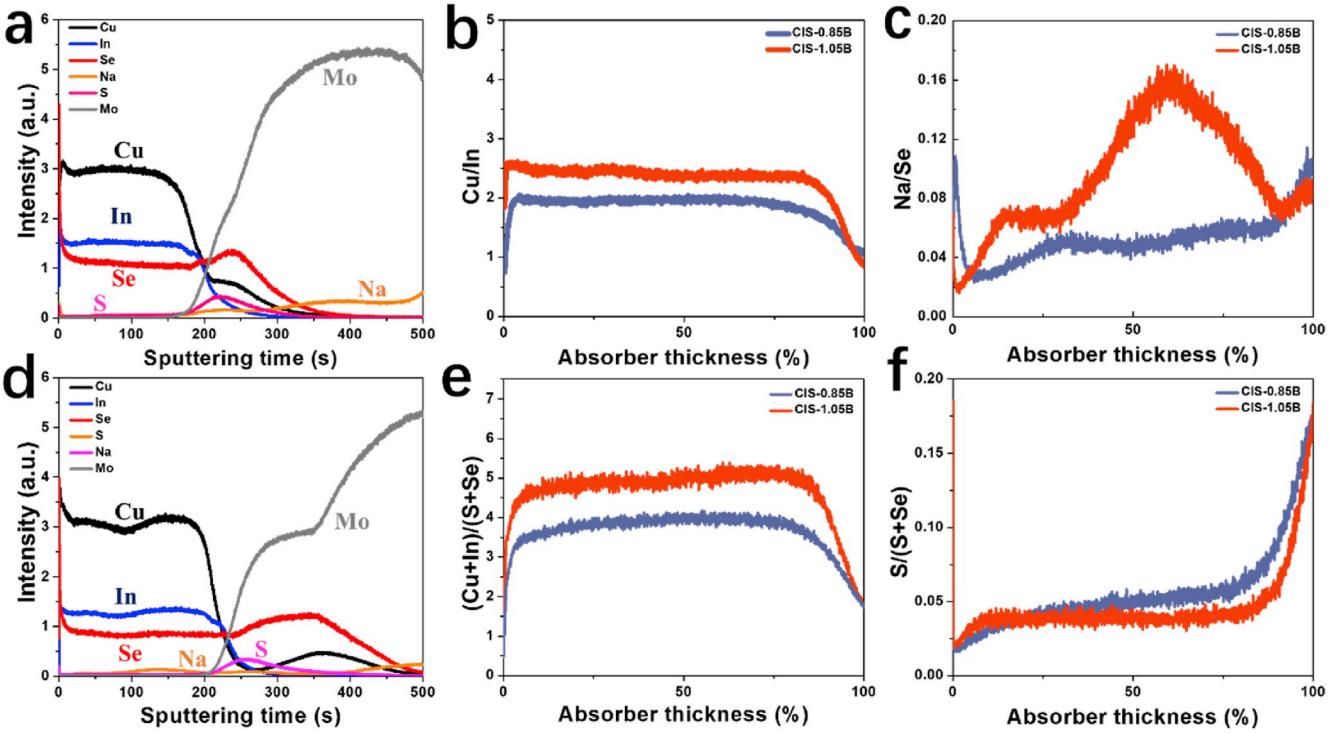

Fig. 4. Composition depth profiles (a, d) and comparison of Cu/In (b), Na/Se (c), (Cu + In)/(S + Se) (e), and S/(S + Se) ratios of CIS-0.85B (a) and CIS-1.05B (d) absorber films measured by GDOES. The X-axis in (b, c, e, and f) is normalized to 100% absorber thickness.

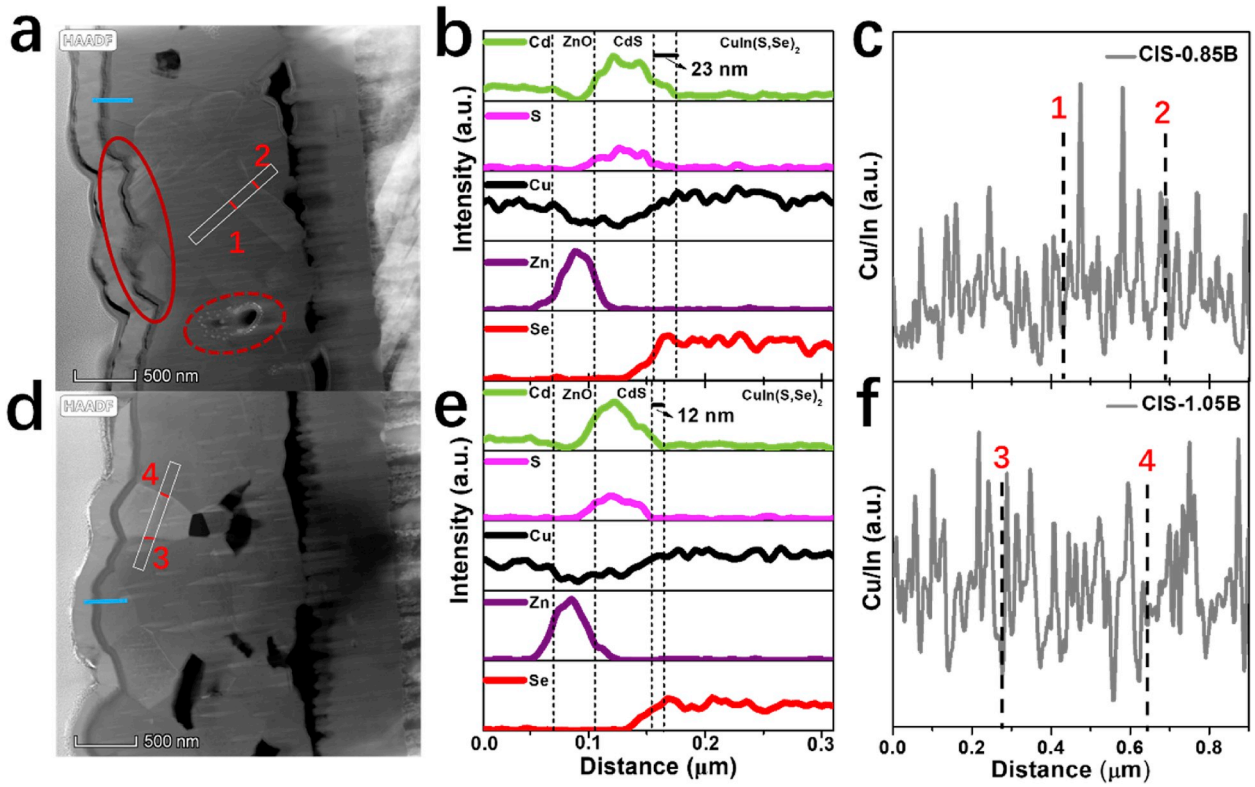

Fig. 5. Dark field TEM images (a, d) and EDX line sans cross CdS/absorber interfaces (the blue lines in a and d) (b, e) and inter grain boundaries (the white rectangles in a and d) (c, f) of absorber films CIS-0.85B (a, b, c) and CIS-1.05B (d, e, f).

condition, near stoichiometric surface composition prevents Cd diffusion, leading to limited Cd penetration. Shorter Cd diffusion depth (and thereby shorter n-type inversion) is beneficial for V_{oc} because of steeper band bending. The band diagrams of both devices in dark and under illumination are illustrated in supporting information (Fig. S6). In addition, inter grain line scans show the [Cu]/[In] ratio near grain boundaries are at the average level (positions 1&2 for CIS-0.85B and 3&4 for CIS-1.05B), indicating no $Cu_{2-x}Se$ impurity at the grain boundaries in Cu-rich absorber fabricated under high pressure selenization. More line scans (Fig. S7) show the [Cu]/[In] ratio at grain boundaries are all at average level.

Fig. 6 shows c-AFM images of CIS-0.85B and CIS-1.05B absorber films. It is noted that the applied sample bias was −2.5 V for CIS-0.85B and −0.75 V for CIS-1.05B for better imaging. It can be clearly seen that the grain boundaries of CIS-0.85B film are more conductive than the grain interior, as generally observed in Cu-poor chalcopyrite absorbers in the literatures [29,30] For CIS-1.05B, on the contrary, the grain interior is more conductive than the grain boundary. Furthermore, the conductivity of CIS-1.05B is much higher than the conductivity of CIS-0.85B even under a smaller bias. For Cu poor chalcopyrite, V_{cu} is believed to account for the p-type conductivity [31,32]. In Cu-rich CIS-1.05B film, more Cu_{In} [33] (which is also a shallow acceptor) may form, thus increasing the carrier concentration and conductivity. Capacitance–voltage (*C–V*) profiling measurements confirmed

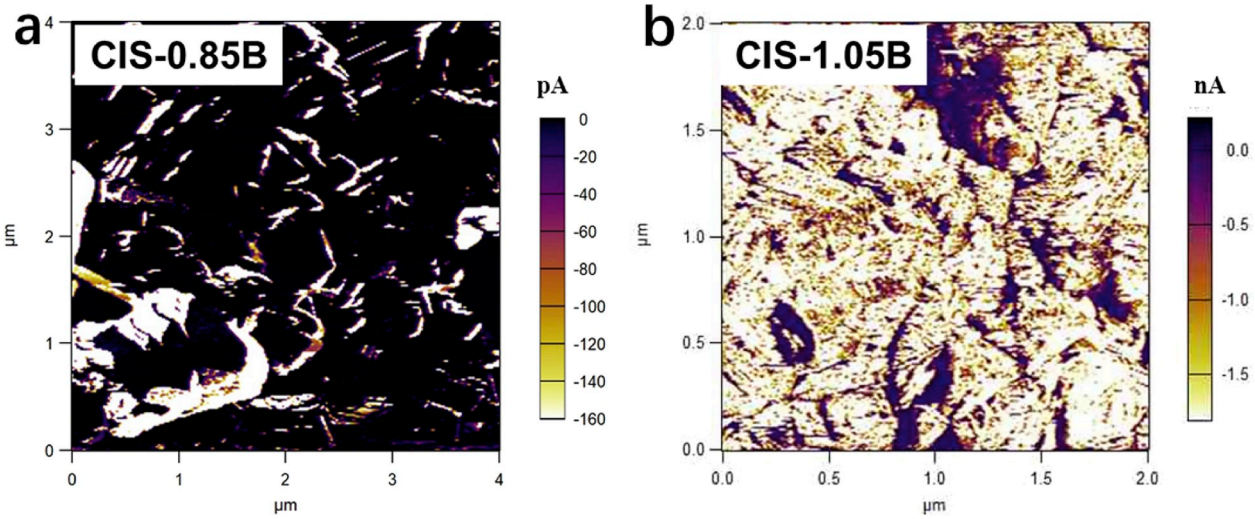

Fig. 6. c-AFM images of CIS-0.85B (a) and CIS-1.05B (b). The applied sample bias was −2.5 V for CIS-0.85B and −0.75 V for CIS-1.05B.

CIS-1.05B has higher carrier concentration than CIS-0.85B (Fig. S8). The rich defective states at grain boundaries might account for the decreased conductivity of grain boundaries in CIS-1.05B film, which needs further investigation.

Fig. 7 shows the temperature-dependent PL spectra of CIS-0.85B and CIS-1.05B absorber films. For the CIS-0.85B film (Fig. 7a), two emissions at 0.853 eV and 0.936 eV are observed at a low temperature of 83 K. With the increasing temperature from 83 K to 263 K, the two peaks show a blue shift and the associated peak intensity gradually decreases. In addition, the peaks for CIS-0.85B film are broad and show an asymmetrical shape, which are typical signatures for Cu-poor absorbers [20,34]. For the CIS-1.05B film (Fig. 7b), only one peak appears at 0.991 eV at 83 K, and with increasing temperature, similar to the CIS-0.85B film, a blue-shift of the peak with decreasing peak intensity is observed. However, compared with the peaks from the CIS-0.85B film, we observe a narrower peak with more symmetrical shape, and the peak position is more blue shifted (0.991 eV for CIS-1.05B film at 83 K vs. 0.853 eV and 0.936 eV for CIS-0.85B film at 83K). Because of the temperature limitation, the excitonic transition for Cu-rich film which generally appears below 50 K is not observed. The peaks for CIS-0.85B film and CIS-1.05B film are all defect related transitions, and the blue shifts of the peak position with the increasing temperature indicate these defects are gradually thermally emptied [35,36]. The broader, more redshifted and more asymmetric emission of CIS-0.85B film is caused by fluctuating potentials due to a higher degree of compensation. This high degree of compensation was caused by large amount of defects such as Cu vacancy and In_{Cu} antisite in the off-stoichiometric composition film [34]. In highly compensated semiconductors the statistical distribution of donors and acceptors leads to areas with an excess of positively charged donors and areas with an excess of negatively charged acceptors. Between these charged areas a spatially fluctuating electrostatic potential is formed [34]. These fluctuating potentials lead to the observed red shift with the decreasing of [Cu]/[In] ratio. The high concentration of charged defects (donors and acceptors) will still be present at room temperature, which will deteriorate the transport properties and thus reduce the device performance. By contrast, the defect concentration for CIS-1.05B film are much lower which is beneficial for device performance.

2.3. Champion solar cells from Cu-rich CISSe and CIGSSe absorbers

With 108 nm ARC, a champion CISSe device with an active area efficiency of 14.5% was achieved from Cu-rich CIS-1.05B absorber with J_{sc} of 38.5 mA/cm^2, V_{oc} of 0.520 V, and *FF* of 72.5%. By using 25% Ga to substitute indium, a champion CIGSSe solar cell with an active area efficiency of 15.2%, J_{sc} of 35.2 mA/cm^2, V_{oc} of 0.604 V, and *FF* of 71.5% was demonstrated by similar fabrication from solution with [Cu]/([In]+[Ga]) = 1.05. The *J-V* and *EQE* curves of the two champion devices are given in Fig. 8. The current density integrated from the *EQE* are 37.1 mA/cm^2 for CISSe and 34.5 mA/cm^2 for CIGSSe solar cell, matching well with those from *J-V* measurements. The band gaps extracted from the *EQE* curves are 1.01 eV for the CISSe and 1.12 eV for the CIGSSe absorber. To the best of our knowledge, 14.5% and 15.2% are record high efficiency for CIS and CIGS solar cells from all non-hydrazine solution approaches. We note the efficiencies are achieved from uniform composition absorber without band gap gradient [37–39], alkali post deposition treatment (PDT) [40–43] and new buffer layer [44,45] that have pushed CIGS to current world record efficiency. Recent reports [46,47] show the effectiveness of PDT is related to the CGI of the absorber layer and PDT can greatly improve absorber doping concentration and reduce defect density of absorber with composition close to stoichiometry. We expect higher device performance can be achieved from our Cu-rich absorber by applying the PDT strategy, which will be our follow-up work.

3. Conclusions

We report highly efficient CISSe and CIGSSe solar cells from Cu-rich absorbers fabricated from DMF molecular solutions. Characterizations including XRD, Raman, SEM and EDX show that selenizing DMF solution processed precursor films with [Cu]/[In] ratio up to 1.05 under high Ar pressure (0.16 MP) enables higher quality chalcopyrite absorber materials with more densely packed grains, smoother surface, and $Cu_{2-x}Se$-free grain boundaries than that under normal Ar pressure (0.10 MP) selenization, resulting in better solar cell performance in every composition investigated. Further composition and electrical property investigation by XRD, Raman, TEM, GDOES, c-AFM and PL and side by side comparison between high pressure selenized Cu-poor CIS-0.85B ([Cu]/[In] = 0.85) and Cu-rich CIS-1.05B ([Cu]/[In] = 1.05) absorbers show that CIS-1.05B film has stoichiometric composition and uniform surface that facilitate more epitaxial-like deposition of overlying CdS and a narrower n-type build-in inversion, higher conductivity and higher Na concentration than CIS-0.85 film. All these improvements greatly reduce interface and bulk recombination and result in CISSe and CIGSSe solar cells with power conversion efficiency up to 14.5% and 15.2%, respectively, which are both the highest efficiency CIS and CIGS devices from non-hydrazine solutions. Our results for the first time demonstrate highly efficient chalcopyrite solar cells from Cu-rich absorbers, which has great potential to further improve solution based chalcopyrite solar cell efficiency.

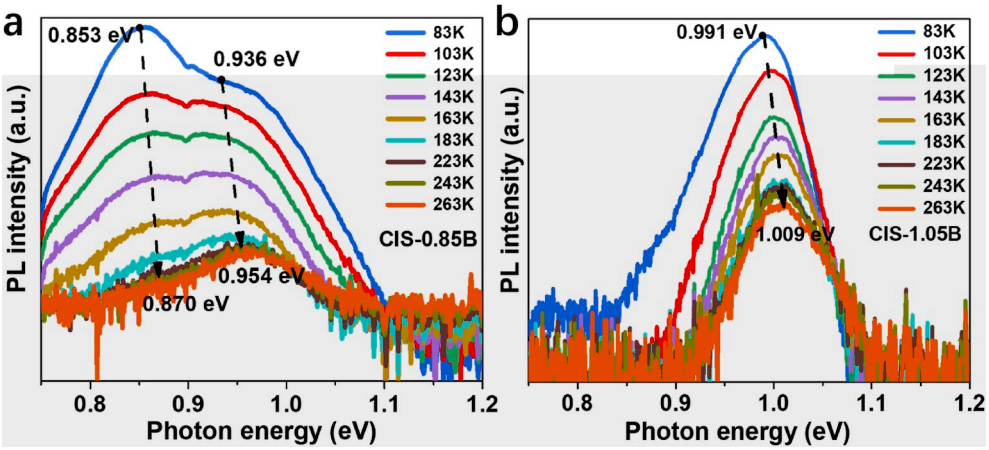

Fig. 7. Temperature dependent PL spectra of CIS-0.85B (a) and CIS-1.05B (b) absorber films.

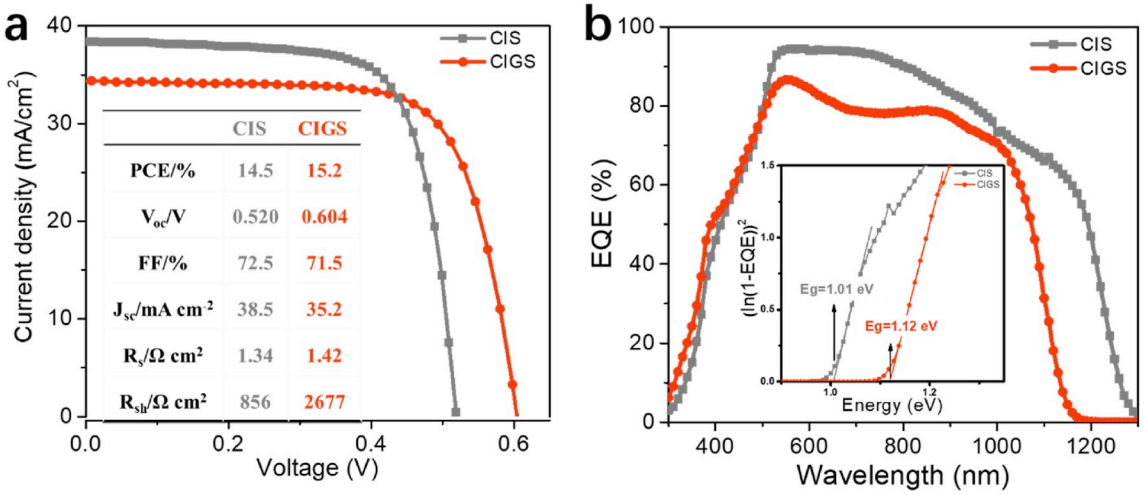

Fig. 8. *J-V* (a) and *EQE* (b) characteristics of the champion CIS and CIGS solar cells with the absorber fabricated from Cu-rich ([Cu]/[In] = 1.05) DMF molecular solutions. Inset of b: extraction of band gap from *EQE*.

4. Experimental section

4.1. Preparation of CIS and CIGS precursor solutions

Precursor solution with [Cu]/[In] = 1.05 was prepared as follow: first, 2.277 g thiourea (TU, 99%, Aladdin, recrystallized) was added into 8 mL DMF under stirring to form a clear solution. Then, 0.505 g CuCl (99.999%, Aldrich) and 1.426 g $InCl_3{\cdot}4H_2O$ (99.99%, Aladdin) were subsequently added to the above solution until completely dissolved. The ratio of CuCl:$InCl_3{\cdot}4H_2O$:Tu was 1.05:1.00:6.15. Precursor solutions with [Cu]/[In] ratios of 0.85, 0.95 and 1.20 were similarly prepared with the molar ratio of [Tu]/([Cu] + [In]) fixed at 3. The CIGS precursor solution was prepared by using 25% $GaCl_3$ (mole ratio) to substitute $InCl_3{\cdot}4H_2O$.

4.2. Fabrication of CIS and CIGS devices

Solar cell devices with a configuration of soda-lime glass/Mo/CISSe (CIGSSe)/CdS/i-ZnO/ITO/Ni/Al were fabricated. First, the precursor solution was spin-coated on Mo coated soda-lime glass substrate at a speed of 4000 rpm for 60 s; the wet film was immediately annealed on a hot plate at a temperature of 340 °C for 1 min. The spin-coating and annealing was repeated for 10 times to reach the desired thickness. The precursor film was then put into a graphite box (7.5 × 3 × 0.6 cm^3) with 0.45 g selenium pellets equally distributed around the edges and corners to react with Se in a tube furnace (so called selenization) and form CISSe (CIGSSe) absorber. The furnace was pumped down to 50 Pa and refilled with Ar three times to guarantee an oxygen-free environment. The selenization was performed at 580 °C for 20 min with two different Ar pressures, 1 atm (0.10 MP, condition A) and 1.6 atm pressure (0.16 MP, condition B), the pressure was controlled by tuning the gas valve. It should be noted that high Ar pressure (1.6 atm.) selenization is *hazard* and need to be conducted properly. After selenization, the film was first soaked in 20% ammonium sulfide ($(NH_4)_2S$) solution for 15 min followed by chemical bath deposition (CBD) of 50 nm CdS buffer layer according to our previous reports [48–50]. Then a window layer consisting of 50 nm i-ZnO and 150 nm ITO was deposited by RF sputtering. The devices were finished by thermal evaporation of Ni/Al top contact grids through a shadow mask. The solar cell area was defined by mechanical scribing and each solar cell has an active area around 0.1 cm^2.

4.3. Film and device characterization

X-ray diffraction (XRD) spectra (2θ scan) were collected by a Siemens D5005 X-ray powder diffraction system using Cu Kα (λ = 1.5406 Å) X-ray as the source at a scan rate of 6°/min. The Raman spectra were acquired on Renishaw inVia microscope using a 532 nm laser diode as the excitation source. The film morphology and elemental composition analysis were measured on Hitachi S4800 scanning electron microscope (SEM). Secondary electrons were used for surface and cross-section imaging measurements at 20 kV, 25 kV acceleration voltage respectively. Using 15 kV and 20 kV power for energy dispersive X-ray (EDX) measurement to obtain the average composition. The ultrathin lamellar were fabricated from the solar cell devices by focused ion beam (FIB) technique on Quanta 3D FEG Dualbeam. Platinum was deposited on the sample surface for protection and connection to the Mo grid. Transmission electron microscopy (TEM) images and elemental analysis of the FIBed samples were measured on FEI TITAN G2 60–300. The current density-voltage (*J-V*) curves of the solar cells were measured at room temperature under 100 mW/cm^2 AM1.5 simulated sunlight using a Keithley 2400 source meter. The external quantum efficiency (*EQE*) were measured on Enlitech QE-R3018 using calibrated Si and Ge diodes (Enli technology Co. Ltd.) as reference. Conducting atomic force microscopy (c-AFM) was performed on an Asylum MFP-3D using Au-coated contact mode tips (Budget Sensors CONTGB-G). The deflection was set to ~200 mV (~20 nm) for all images, and the bias listed is applied to the sample relative to the tip. The *C–V* characterizations curves were obtained using an FT-1030 HERA DLTS system configured with a JANIS VPF-800 cryostat controller. The *C–V* curves were obtained in the range from −1 to 0 V. Composition profiles of the films were taken using a GD Profiler 2 (Horiba Jobin Yvon) using a 4 mm anode and high-power radio frequency (RF) argon plasma. Emission spectra were collected using a polychromator and the following emission lines, 325 nm for copper, 451 nm for indium, 181 nm for sulfur, 196 nm for selenium, 386 nm for molybdenum, and 590 nm for sodium.

Notes

The authors declare no competing financial interests.

Declaration of competing interest

The authors declare that they have no known competing financial interests or personal relationships that could have appeared to influence the work reported in this paper.

Acknowledgements

This work was supported primarily by the National Natural Science Foundation of China (NSFC, Grant No. 21571106). We acknowledge the support from the Synergetic Innovation Centre for Organic Electronics and Information Displays. J.J.J. and S.T.Y. acknowledges the support from Postgraduate Research and Practice Innovation Program of Jiangsu Province. R.G. and E.J. acknowledge support of facilities in the Molecular Analysis Facility, a National Nanotechnology Coordinated Infrastructure site at the University of Washington which is supported in part by the National Science Foundation (grant NNCI-1542101), the University of Washington, the Molecular Engineering & Sciences Institute, the Clean Energy Institute, and the National Institutes of Health. X.H., K. S. and M.A.G acknowledge the support from Australian Renewable Energy Agency (grant RND011). J.J.J. thanks S.J.Y. (Henan University) for the *C–V* measurement.

Appendix A. Supplementary data

Supplementary data to this article can be found online at https://doi.org/10.1016/j.nanoen.2019.104438.

References

[1] Solar Frontier press release, Solar Frontier Achieves World Record Thin-Film Solar Cell Efficiency of 23.35%, 2019-01-17. http://www.solar-frontier.com/eng/news/2019/0117_press.html. (Accessed 15 April 2019).

[2] R. Kamada, T. Yagioka, S. Adachi, A. Handa, K.F. Tai, T. Kato, H. Sugimoto, New world record Cu(In,Ga)(Se,S)$_2$ thin film solar cell efficiency beyond 22%, in: Proceedings of the 43rd IEEE Photovoltaic Specialists Conference, 2016, pp. 1287–1291, https://doi.org/10.1109/PVSC.2016.7749822.

[3] M. Nakamura, N. Yoneyama, K. Horiguchi, Y. Iwata, K. Yamaguchi, H. Sugimoto, T. Kato, Resent R&D progress in solar frontier's small-sized Cu(In,Ga)(Se,S)$_2$ solar cells, in: Proceedings of the 40th IEEE Photovoltaic Specialist Conference, 2014, https://doi.org/10.1109/PVSC.2014.6925346, 0107–0110.

[4] C.J. Hages, M.J. Koeper, C.K. Miskin, K.W. Brew, R. Agrawal, Controlled grain growth for high performance nanoparticle-based kesterite solar cells, Chem. Mater. 28 (2016) 7703–7714, https://doi.org/10.1021/acs.chemmater.6b02733.

[5] B.D. Chernomordik, P.M. Ketkar, A.K. Hunter, A.E. Beland, D.D. Deng, E.S. Aydil, Microstructure evolution during selenization of Cu_2ZnSnS_4 colloidal nanocrystal coatings, Chem. Mater. 28 (2016) 1266–1276, https://doi.org/10.1021/acs.chemmater.5b02462.

[6] F.O. Adurodija, J. Song, S.D. Kim, S.H. Kwon, S.K. Kim, K.H. Yoon, B.T. Ahn, Growth of CuInSe$_2$ thin films by high vapour Se treatment of Co-sputtered Cu-In alloy in a graphite container, Thin Solid Films 338 (1999) 13–19, https://doi.org/10.1016/s0040-6090(98)00358-7.

[7] T. Wada, N. Kohara, T. Negami, M. Nishitani, Growth of CuInSe$_2$ crystals in Cu-Rich Cu-In-Se thin films, J. Mater. Res. 12 (1997) 1456–1462, https://doi.org/10.1557/jmr.1997.0200.

[8] R. Mainz, A. Weber, H. Rodriguez-Alvarez, S. Levcenko, M. Klaus, P. Pistor, R. Klenk, H.-W. Schock, Time-resolved investigation of Cu(In,Ga)Se$_2$ growth and Ga gradient formation during fast selenisation of metallic precursors, Prog. Photovoltaics 23 (2015) 1131–1143, https://doi.org/10.1002/pip.2531.

[9] T. Rissom, R. Mainz, C.A. Kaufmann, R. Caballero, V. Efimova, V. Hoffmann, H.-W. Schock, Examination of growth kinetics of copper rich Cu(In,Ga)Se$_2$-films using synchrotron energy dispersive X-ray diffractometry, Sol. Energy Mater. Sol. Cells 95 (2011) 250–253, https://doi.org/10.1016/j.solmat.2010.05.007.

[10] T. Bertram, V. Depredurand, S. Siebentritt, Electrical characterization of defects in Cu-rich grown CuInSe$_2$ solar cells, Ieee J. Photovoltaics 6 (2016) 546–551, https://doi.org/10.1109/jphotov.2015.2508239.

[11] Y. Aida, V. Depredurand, J.K. Larsen, H. Arai, D. Tanaka, M. Kurihara, S. Siebentritt, Cu-rich CuInSe$_2$ solar cells with a Cu-poor surface, Prog. Photovolt. Res. Appl. 23 (2015) 754–764, https://doi.org/10.1002/pip.2493.

[12] M. Buffiere, A.-A. El Mel, N. Lenaers, G. Brammertz, A.E. Zaghi, M. Meuris, J. Poortmans, Surface cleaning and passivation using $(NH_4)_2S$ treatment for Cu(In,Ga)Se$_2$ solar cells: a safe alternative to KCN, Adv. Energy Mater. 5 (2015) 1401689, https://doi.org/10.1002/aenm.201401689.

[13] H. Marko, L. Arzel, A. Darga, N. Barreau, S. Noel, D. Mencaraglia, J. Kessler, Influence of Cu off-stoichiometry on wide band gap CIGSe solar cells, Thin Solid Films 519 (2011) 7228–7231, https://doi.org/10.1016/j.tsf.2010.12.174.

[14] J. Kois, S. Bereznev, O. Volobujeva, E. Mellikov, Electrochemical etching of copper indium diselenide surface, Thin Solid Films 515 (2007) 5871–5875, https://doi.org/10.1016/j.tsf.2006.12.157.

[15] J. Jiang, S. Yu, Y. Gong, H. Xin, 10.3% efficient CuIn(S,Se)$_2$ solar cells from DMF molecular solution with the absorber selenized under high argon pressure, in: Proceedings of the 7th IEEE World Conf. On Photovoltaic Energy Conversion (WCPEC)/A Joint Conf. of 45th IEEE PVSC/28th PVSEC/34th EU PVSEC, 2018, https://doi.org/10.1109/PVSC.2018.8548027, 0831-0834.

[16] J. Jiang, S. Yu, Y. Gong, W. Yan, R. Zhang, S. Liu, W. Huang, H. Xin, 10.3% efficient CuIn(S,Se)$_2$ solar cells from DMF molecular solution with the absorber selenized under high argon pressure, Sol. RRL 6 (2018), https://doi.org/10.1002/solr.201800044, 1800044.

[17] A.R. Uhl, A. Rajagopal, J.A. Clark, A. Murray, T. Feurer, S. Buecheler, A.K.Y. Jen, H.W. Hillhouse, Solution-processed low-bandgap CuIn(S,Se)$_2$ absorbers for high-efficiency single-junction and monolithic chalcopyrite-perovskite tandem solar cells, Adv. Energy Mater. 8 (2018), 1801254, https://doi.org/10.1002/aenm.201801254.

[18] U.C. Boehnke, G. Kuhn, Phase-relations in the ternary-system Cu-In-Se, J. Mater. Sci. 22 (1987) 1635–1641, https://doi.org/10.1007/bf01132385.

[19] S.B. Zhang, S.H. Wei, A. Zunger, H. Katayama-Yoshida, Defect physics of the CuInSe$_2$ chalcopyrite semiconductor, Phys. Rev. B 57 (1998) 9642–9656, https://doi.org/10.1103/PhysRevB.57.9642.

[20] D.-Y. Lee, J. Kim, Characterization of sprayed CuInS$_2$ films by XRD and Raman spectroscopy measurements, Thin Solid Films 518 (2010) 6537–6541, https://doi.org/10.1016/j.tsf.2010.03.062.

[21] E. Rudigier, B. Barcones, I. Luck, T. Jawhari-Colin, A. Perez-Rodriguez, R. Scheer, Quasi real-time Raman studies on the growth of Cu-In-S thin films, J. Appl. Phys. 95 (2004) 5153–5158, https://doi.org/10.1063/1.1667009.

[22] D.M. Xu, K. Pan, X.W. Liu, X.J. Wang, W.Z. Wang, C.J. Liang, Z. Wang, Raman and visible-near infrared spectra of Cu(InGa)Se$_2$ films, Spectrosc. Spectr. Anal. 36 (2016) 3197–3201, https://doi.org/10.3964/j.issn.1000-0593(2016)10-3197-05.

[23] F. Jiang, J. Feng, First principles calculation on polytypes of ordered defect compound $CuIn_5Se_8$, Appl. Phys. Lett. 89 (2006) 221920, https://doi.org/10.1063/1.2399941.

[24] Z.K. Yuan, S.Y. Chen, Y. Xie, J.S. Park, H.J. Xiang, X.G. Gong, S.H. Wei, Na-diffusion enhanced p-type conductivity in Cu(In, Ga)Se$_2$: a new mechanism for efficient doping in semiconductors, Adv. Energy Mater. 6 (2016) 7, https://doi.org/10.1002/aenm.201601191.

[25] P.-P. Choi, O. Cojocaru-Miredin, R. Wuerz, D. Raabe, Comparative atom probe study of Cu(In,Ga)Se$_2$ thin-film solar cells deposited on soda-lime glass and mild steel substrates, J. Appl. Phys. 110 (2011) 124513, https://doi.org/10.1063/1.3665723.

[26] R.V. Forest, E. Eser, B.E. McCandless, J.G. Chen, R.W. Birkmire, Reversibility of (Ag,Cu)(In,Ga)Se$_2$ electrical properties with the addition and removal of Na: role of grain boundaries, J. Appl. Phys. 117 (2015) 115102, https://doi.org/10.1063/1.4915334.

[27] D. Rudmann, A.F. da Cunha, M. Kaelin, F. Kurdesau, H. Zogg, A.N. Tiwari, G. Bilger, Efficiency enhancement of Cu(In,Ga)Se$_2$ solar cells due to post-deposition Na incorporation, Appl. Phys. Lett. 84 (2004) 1129–1131, https://doi.org/10.1063/1.1646758.

[28] T. Nakada, Nano-structural investigations on Cd-doping into Cu(In,Ga)Se$_2$ thin films by chemical bath deposition process, Thin Solid Films 361 (2000) 346–352, https://doi.org/10.1016/s0040-6090(99)00767-1.

[29] D. Azulay, O. Millo, I. Balberg, H.W. Schock, I. Visoly-Fisher, D. Cahen, Current routes in polycrystalline CuInSe$_2$ and Cu(In,Ga)Se$_2$ films, Sol. Energy Mater. Sol. Cells 91 (2007) 85–90, https://doi.org/10.1016/j.solmat.2006.08.006.

[30] T.-P. Hsieh, C.-C. Chuang, C.-S. Wu, J.-C. Chang, J.-W. Guo, W.-C. Chen, Effects of residual copper selenide on CuInGaSe$_2$ solar cells, Solid State Electron. 56 (2011) 175–178, https://doi.org/10.1016/j.sse.2010.11.019.

[31] L.E. Oikkonen, M.G. Ganchenkova, A.P. Seitsonen, R.M. Nieminen, Formation, migration, and clustering of point defects in CuInSe$_2$ from first principles, J. Phys. Condens. Matter 26 (2014) 13, https://doi.org/10.1088/0953-8984/26/34/345501.

[32] J. Ramanujam, U.P. Singh, Copper indium gallium selenide based solar cells - a review, Energy Environ. Sci. 10 (2017) 1306–1319, https://doi.org/10.1039/c7ee00826k.

[33] J.-S. Park, S. Kim, Z. Xie, A. Walsh, Point defect engineering in thin-film solar cells, Nat. Rev. Mater. 3 (2018) 194–210, https://doi.org/10.1038/s41578-018-0026-7.

[34] S. Siebentritt, L. Gütay, D. Regesch, Y. Aida, V. Deprédurand, Why do we make Cu(In,Ga)Se$_2$ solar cells non-stoichiometric? Sol. Energy Mater. Sol. Cells 119 (2013) 18–25, https://doi.org/10.1002/pssc.200404845.

[35] A. Bauknecht, S. Siebentritt, J. Albert, M.C. Lux-Steiner, Radiative recombination via intrinsic defects in $Cu_xGa_ySe_2$, J. Appl. Phys. 89 (2001) 4391–4400, https://doi.org/10.1063/1.1357786.

[36] H. Tanino, T. Maeda, H. Fujikake, H. Nakanishi, S. Endo, T. Irie, Raman-Spectra of CuInSe$_2$, Phys. Rev. B 45 (1992) 13323–13330, https://doi.org/10.1103/PhysRevB.45.13323.

[37] T. Klinkert, T. Hildebrandt, M. Jubault, F. Donsanti, J.F. Guillemoles, N. Naghavi, Adaptation of the surface-near Ga content in Co-evaporated Cu(In,Ga)Se$_2$ for CdS versus Zn(S,O)-based buffer layers, Thin Solid Films 582 (2015) 295–299, https://doi.org/10.1016/j.tsf.2014.09.074.

[38] J. Gong, Y. Kong, J. Li, K. Wang, X. Wang, Z. Zhang, Z. Ding, X. Xiao, Enhancing photocurrent of Cu(In,Ga)Se$_2$ solar cells with actively controlled Ga grading in the absorber layer, Nano Energy 62 (2019) 205–211, https://doi.org/10.1016/j.nanoen.2019.05.052.

[39] Q. Fan, Q. Tian, H. Wang, F. Zhao, J. Kong, S. Wu, Regulating the starting location of front-gradient enabled highly efficient Cu(In,Ga)Se$_2$ solar cells via a facile thiol-amine solution approach, J. Mater. Chem. 6 (2018) 4095–4101, https://doi.org/10.1039/c7ta10889c.

[40] X.S. Wang, Q.M. Fan, Q.W. Tian, Z.J. Zhou, D.X. Kou, W.H. Zhou, Q.B. Meng, Z. Zheng, S.X. Wu, Cu(In,Ga)Se$_2$ thin-film solar cells with 11.5% efficiency: an effective and low-cost way of Na-incorporation for grain-growth, Sol. Energy 185 (2019) 34–40, https://doi.org/10.1016/j.solener.2019.04.051.

[41] S. Kim, H. Tampo, H. Shibata, K. Matsubara, S. Niki, Effect of combined alkali (KF plus CsF) post-deposition treatment on Cu(InGa)Se_2 solar cells, Phys. Status Solidi RRL 12 (2018), 1800372, https://doi.org/10.1002/pssr.201800372.
[42] R. Wuerz, W. Hempel, P. Jackson, Diffusion of Rb in polycrystalline Cu(In, Ga)Se_2 layers and effect of Rb on solar cell parameters of Cu(In, Ga)Se_2 thin-film solar cells, J. Appl. Phys. 124 (2018), 165305, https://doi.org/10.1063/1.5044629.
[43] M. Raghuwanshi, A. Vilalta-Clemente, C. Castro, S. Duguay, E. Cadel, P. Jackson, D. Hariskos, W. Witte, P. Pareige, Influence of RbF post deposition treatment on heterojunction and grain boundaries in high efficient (21.1%) Cu(In,Ga)Se_2 solar cells, Nano Energy 60 (2019) 103–110, https://doi.org/10.1016/j.nanoen.2019.03.028.
[44] T.M. Friedlmeier, P. Jackson, A. Bauer, D. Hariskos, O. Kiowski, R. Wuerz, M. Powalla, Improved photocurrent in Cu(In, Ga)Se_2 solar cells: from 20.8% to 21.7% efficiency with CdS buffer and 21.0% Cd-free, Ieee J. Photovoltaics 5 (2015) 1487–1491, https://doi.org/10.1109/jphotov.2016.2520213.
[45] T. Hildebrandt, M. Kozolinsky, N. Loones, M. Bouttemy, J. Vigneron, A. Etcheberry, D. Lincot, F. Donsanti, N. Naghavi, Fast chemical bath deposition process at room temperature of ZnS-based materials for buffer application in high-efficiency Cu(In, Ga)Se_2-based solar cells, Ieee J. Photovoltaic 8 (2018) 1862–1867, https://doi.org/10.1109/jphotov.2018.2871601.
[46] T. Kodalle, T. Bertram, R. Schlatmann, C.A. Kaufmann, Effectiveness of an RbF post deposition treatment of CIGS solar cells in dependence on the Cu content of the absorber layer, Ieee J. Photovoltaics 9 (2019) 1839–1845, https://doi.org/10.1109/JPHOTOV.2019.2929418.
[47] T. Feurer, R. Carron, G.T. Sevilla, F. Fu, S. Pisoni, Y.E. Romanyuk, S. Buecheler, A. N. Tiwari, Efficiency improvement of near-stoichiometric $CuInSe_2$ solar cells for application in tandem devices, Adv. Energy Mater. 9 (2019), 1901428, https://doi.org/10.1002/aenm.201901428.
[48] H. Xin, J.K. Katahara, I.L. Braly, H.W. Hillhouse, 8% efficient $Cu_2ZnSn(S,Se)_4$ solar cells from redox equilibrated simple precursors in DMSO, Adv. Energy Mater. 4 (2014), 1301823, https://doi.org/10.1002/aenm.201301823.
[49] H. Xin, S.M. Vorpahl, A.D. Collord, I.L. Braly, A.R. Uhl, B.W. Krueger, D.S. Ginger, H.W. Hillhouse, Lithium-doping inverts the nanoscale electric field at the grain boundaries in $Cu_2ZnSn(S,Se)_4$ and increases photovoltaic efficiency, Phys. Chem. Chem. Phys. 17 (2015) 23859–23866, https://doi.org/10.1039/c5cp04707b.
[50] S. Wu, J. Jiang, S. Yu, Y. Gong, W. Yan, H. Xin, W. Huang, Over 12% efficient low-bandgap $CuIn(S, Se)_2$ solar cells with the absorber processed from aqueous metal complexes solution in air, Nano Energy 62 (2019) 818–822, https://doi.org/10.1016/j.nanoen.2019.06.010.

Jingjing Jiang is currently pursuing his Ph.D. under the supervision of Prof. Hao Xin in the School of Materials Science and Engineering at Nanjing University of Posts and Telecommunications, China. He received his B.S. in the School of Materials Science and Engineering (2015) at Changchun University of Science and Technology, China. His current research interests focus on solution processed Cu(In,Ga)Se_2 solar cells.

Rajiv Giridharagopal is as Senior Research Scientist at the University of Washington. He received a B.S. with high honors from the University of Texas at Austin in 2004 and M.S. and Ph. D. degrees from Rice University in 2007 and 2010, all in electrical engineering. His graduate work was supported by a NSF graduate research fellowship. Prior to his current position, he was a postdoctoral fellow in David Ginger's lab followed by a position at Intel Corp. in optical microscopy development.

Erin Jedlicka is a graduate student at the University of Washington pursuing a Ph.D. in Chemistry. She received a B.S. with honors in Chemistry from the United States Naval Academy in 2012 and a M.S. in Chemistry from the University of Washington in 2017.

Kaiwen Sun received his B.S., M.S. from Central South University, China in 2011 and 2014; Ph.D degree from University of New South Wales (UNSW), Australia in 2018. After that, he worked as a postdoctoral fellow at the Australian Centre for Advanced Photovoltaics in School of Photovoltaic and Renewable Energy Engineering, UNSW. His research interests are thin film solar cells including kesterite, chalcogenide and perovskite photovoltaic technology.

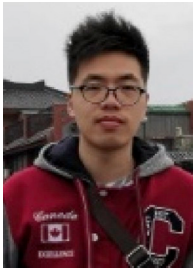

Shaotang Yu received his B.S. degree in Optical Information Science and Technology in 2015 from China University of Petroleum, Tsingtao, China, and his M.S. degree in Optical Engineering in 2018 from Nanjing University of Posts and Telecommunications, Nanjing, China. From September 2018 he becomes a graduate student in Nanjing University of Posts and Telecommunications for a Ph.D. degree. His current research is precursor solution-based CIS/CIGS thin film solar cells.

Sanping Wu joined Prof. Hao Xin's group in 2017 and is a M.S. candidate supervised by Prof. Hao Xin at Department of Materials Science and Engineering, Nanjing University of Posts and Telecommunications, China. He obtained his B.S. degree in Applied Chemistry from Yanshan University, China in 2017. His current M.S. research is focusing on solution processing of CIGS solar cells.

Yuancai Gong is a Ph.D. candidate and study about thin film solar cells at Institute of Advanced Materials, School of Materials Science and Engineering, Nanjing University of Posts & Telecommunications. His research focuses on earth-abundant kesterite thin film solar cells.

Weibo Yan obtained his Ph.D. degree in organic chemistry from Nankai University in 2011. After that, he worked as a postdoctoral fellow in organic nanostructures at Karlsruhe Institute of Technology (KIT) in Germany from 2011 to 2012. From 2013 to 2016, Weibo worked as a postdoctoral fellow in Peking University on the synthesis of solar cell materials and the fabrication of their devices. He is currently a lecturer in Nanjing University of Posts and Telecommunications. His research focuses on photovoltaic devices including perovskite and organic solar cells.

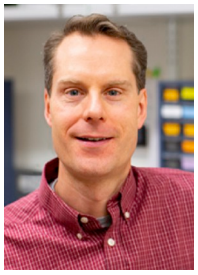

David S. Ginger is the Alvin L. and Verla R. Kwiram Professor of Chemistry at the University of Washington, a Washington Research Foundation Distinguished Scholar, and Chief Scientist of the University of Washington Clean Energy Institute. He earned dual B.S. degrees in chemistry and physics from Indiana University in 1997 and a Ph.D. in physics from the University of Cambridge (U.K.) in 2001. After a postdoctoral fellowship at Northwestern University, he joined the University of Washington in 2003. Further information can be found online at http://depts.washington.edu/gingerlb/.

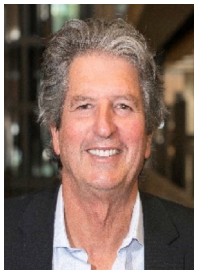

Martin Green is Scientia Professor at the University of New South Wales, Sydney and Director of the Australian Centre for Advanced Photovoltaics, involving several other Australian Universities and research groups. His group's contributions to photovoltaics include inventing the PERC cell, now the main commercial solar cell, and holding the record for silicon cell efficiency for 30 of the last 37 years, described as a "Top Ten" Milestones in solar photovoltaics history. Major international awards include the 1999 Australia Prize, the 2002 Right Livelihood Award, also known as the Alternative Nobel Prize, and the 2018 Global Energy Prize presented in Moscow.

Xiaojing Hao is Associate Professor and Scientia Fellow at the School of Photovoltaic and Renewable Energy Engineering, University of New South Wales (UNSW), Australia. She received her Ph.D. degree from UNSW in 2010, where she then worked as a research fellow (2010–2014) and a senior lecturer (2015–2018). Hao's research focuses on the design of thin film solar cells and tandem solar cells, and the development of thin film energy materials for solar fuel application.

Dr Huang Wei received his PhD from Peking University. In 2001, he was appointed as a chair professor at Fudan University, founded and chaired the Institute of Advanced Materials. Afterwards, he became the deputy president of Nanjing University of Posts & Telecommunications, and then president of Nanjing Tech University. He is the deputy president and provost of Northwestern Polytechnical University. He was elected as Academician of Chinese Academy of Sciences in 2011. His research includes organic/flexible electronics, especially, organic/plastic materials and devices, nanomaterials, etc. He has published over 700 journal publications with SCI citations over 71,000 and h-index of 117.

Hao Xin is currently a professor of College of Materials Science and Engineering at the Nanjing University of Posts and Telecommunications. She received her Ph.D. from Peking University in 2003. From 2003 to 2006, she worked as a JST CREST researcher at NIMS and a JSPS fellow at JAIST in Japan. Then she moved to USA and worked as an associate researcher and research scientist until 2012 in the Department of Chemical Engineering, University of Washington. Her current research mainly focuses on solution processed thin film photovoltaics including CZTS, CIGS, OPVs, and perovskite solar cells.